Experimental Thermal and Fluid Science 92 (2018) 46–55

Contents lists available at ScienceDirect

Experimental Thermal and Fluid Science

journal homepage: www.elsevier.com/locate/etfs

A novel water hammer device designed to produce controlled bubble collapses

Juan M. Rosselló[a,c,*], Raúl Urteaga[a,d], Fabián J. Bonetto[a,b,c]

[a] Consejo Nacional de Investigaciones Científicas y Técnicas (CONICET), Argentina
[b] Comisión Nacional de Energía atómica, Centro Atómico Bariloche, Río Negro, Argentina
[c] Laboratorio de Cavitación y Biotecnología, Instituto Balseiro – Universidad Nacional de Cuyo, Río Negro, Argentina
[d] Instituto de Física del Litoral (IFIS – Litoral), Santa Fe, Argentina

ARTICLE INFO

Keywords:
Water hammer
Forced bubble collapse
Magnetic actuator

ABSTRACT

In this work, a novel prototype of a water hammer device designed to produce controlled collapses of a single cavitation bubble is presented. It employs a new driving method in which a laser generated bubble is initially expanded and subsequently compressed using an electromechanical piston. It brings the possibility of reaching high energy concentrations in the collapses and allows the independent control of the most relevant system parameters. In this way, a higher control over the bubble dynamics is obtained compared to the typically reported in acoustically driven systems, laser cavitation or a conventional water hammer. This device constitutes a proof of concept in a series of low energy trials performed using glycerin and phosphoric acid as working liquids. Simulations of the bubble dynamics for prototypical cases were performed in order to extend the experimental results. We found that the most relevant parameter related to collapse strength is the expansion ratio, i.e. the radius of the expanded bubble (before compression) over the equilibrium bubble radius. The results clearly indicate that this driving strategy has a great potential to produce high energy bubble collapses.

1. Introduction

The experimental study of strongly collapsing cavitation bubbles is still a very interesting and challenging subject [1]. Despite recent advances in non linear bubble dynamics related to the amount of energy concentrated on the bubble collapse [2–4], there is still potential to increase the compression ratio in order to achieve a higher temperature plasma (e.g. of hundred thousand degrees).

The use of a focused laser pulse to "seed" bubbles in a fluid has become a standard technique in cavitation studies due to its versatility of application in different types of experimental set ups [3,5–16]. Laser-induced bubbles (LIB) can be generated either in a static pressure liquid environment [7,9,17], immersed in a stationary sound pressure field [19–21], or in a system with transient pressure variations [22]. In the first case, the abrupt expansion of the gas volume induced by the laser pulse heating is followed by a inertial collapse, strong enough to generate luminescence pulses. As described in studies from Ohl, Wolfrum and Li [5,8,15], experiments performed in water showed a strong dependence on intrinsic parameters of LIB bubbles, such as the equilibrium radius (R_0), the maximum radius (R_{max}), the collapse time (t_c), the mechanical energy density and the intensity of the light pulses (I_L), with the static pressure (p_0) and the laser pulse energy.

The shape stability of LIB bubbles is limited in cases with laser pulse energies above a certain threshold. Also, the initial laser pulse anisotropy [23] and the large radius of LIB bubbles influence their shape stability. Under these circumstances, viscosity and surface tension effect is not sufficient to stabilize the interface before collapse, thus surface waves are developed causing bubbles to break during collapse due to the Rayleigh–Taylor instability (RTI) [6,7].

One way to improve bubble collapse intensity was found in a phenomenon known as "water hammer" [24]. In this process, the collapse of one or more bubbles is forced by a sudden increase of the pressure of a liquid column (containing the bubbles), produced by an abrupt arrest of the fluid (Joukowsky's pressure). When the phenomenon is violent enough, the compressed bubbles can emit high-intensity light pulses. In recent years, devices based on this technique have been studied using different fluids [2,25]. In those where sulfuric acid or phosphoric acid were used, the emitted light intensity was of up to five orders of magnitude higher than when water was used [25]. A relevant aspect of these systems is that the dynamics of the bubbles is governed by the hammer dynamics [26]. This implies that, as it occurs in acoustic-driven bubbles, it is impossible to modify the experimental parameters

* Corresponding author at: Consejo Nacional de Investigaciones Científicas y Técnicas (CONICET), Argentina.
E-mail address: jrossello@cab.cnea.gov.ar (J.M. Rosselló).

https://doi.org/10.1016/j.expthermflusci.2017.11.016
Received 22 June 2017; Received in revised form 12 October 2017; Accepted 19 November 2017
Available online 21 November 2017

independently without disrupting the balance that keeps bubbles emitting light. Besides, the shock and rarefaction waves developed in the liquid column induce the appearance of multiple bubbles absorbing a significant part of the available mechanical energy. Also, the fluid movement and the proximity of the bubbles to the tube wall cause a deformation from the spherical shape of the bubbles [11,27] leading to bubble rupture due to the shape instability (RTI). Moreover, in this type of design the displacement of the bubbles together with the hammer tube makes it difficult to acquire the temporal evolution of the bubble radius ($R(t)$). In order to achieve strong collapses and high temperature plasma in liquid hammer-type systems, large accelerations of the liquid column are required, thus its inertia (added to the one of the mechanical device) poses a major technical challenge. Recently, Ramsey et al. [3] produced luminescence from the rapid compression of a bubble in water by means of piezoelectric actuators. In this study, the bubble was compressed to its the minimum radius (R_{min}) from its ambient radius. Considering that the mechanical energy density developed in the collapse is proportional to $(R_{max}/R_{min})^3$, the expansion of the bubble prior to its collapse is a key factor to upscale the energy concentration.

In acoustically driven systems like sonoluminescence (SBSL), the periodic oscillations of the bubbles are commonly affected by a positional instability, which imposes an upper threshold in the applied acoustic pressure, a spatial instability, which produces moving-bubbles in viscous liquids, and a parametric shape instability. These factors impose a limit in the focused energy and also interfere with the measurement process.

In this work we present an alternative approach to the traditional liquid hammer, designed to produce and study controlled bubble collapses, with the potential to overcome the limitations mentioned above. The primary objective of this prototype is to establish a new methodology to achieve strong collapses of a single bubble with a energy concentration higher than those reported so far in SBSL, by independently controlling fundamental bubble parameters, namely R_{max},R_0, the expansion and compression pressures (p_0^{min} and p_0^{max}) and t_c. In what follows, we will refer to as *Single forced bubble collapse* (SFBC) to the particular case in which a bubble is expanded by a negative pressure (traction applied to the liquid) and then suddenly compressed boosting its collapse. In SFBC experiments both the liquid and the bubble remain fixed during a single collapse. The main advantages of this design are the ability to control a significant number of parameters in a completely independent way, and the absence of positional instability and spatial instabilities, features not present in the water hammer devices reported to date.

2. Experimental method

In this section, the design, construction and characterization of the SFBC device are presented. It works in three stages. Initially, a bubble is seeded by laser cavitation into the interior of a expansion/compression chamber. Then it is expanded through the traction generated by a piston acting on the liquid and finally, a sudden compression of the fluid is achieved by hitting the piston with a projectile, inducing the bubble collapse.

2.1. Description of the SFBC prototype

A detailed description of the experimental device is presented in Figs. 1 and 2. The centerpiece consisted of a Pyrex glass tube filled with liquid, sealed by two stainless steel pistons (304L) mounted at both ends of the tube. These pistons could be displaced through the tube to exert a traction or compression force onto the fluid. One of the pistons was fixed to an optical table (from now on the "lower" piston). The second one ("upper" piston), could be moved vertically producing a pressure variation inside the cylindrical vessel. The driving force (~ 80 N) was generated by a electromagnetic actuator and transmitted to the upper piston through a series of permanent magnets (NdFeB) (as shown in Fig. 1). The axial force exerted by the actuator coil could be both attractive or repulsive, and its driving signal of an arbitrary shape. The position of the upper piston was determined by using an infrared photosensor (see Fig. 1 (c)). The magnetic rod (10 cm long, 238 g of mass) had a pattern of grooves designed to avoid the loss of energy by inductive effects. In Fig. 1(a) and (b) and Fig. 2 a detailed view of the device structure is shown. The latter was assembled with four triangular plates of 26 cm in its sides with a circular hole of ~ 6 cm in diameter in their centers (see Fig. 1(b)). The plate holding the actuator coil was made of plywood in order to avoid the formation of eddy currents on it.

The magnetic actuator coil was powered with a brand *Bosch S455D* battery (Max. curr. CA = 620 A, Energy 55 A h, Volt. 12.6 V_{CC}, Resistance $R_{Batt} \approx 9\,m\Omega$). This type of energy source has a high discharge velocity, which makes it suitable to generate high current pulses with a short actuator response time (~ 2.5 ms), which is the time it takes for the electromagnet to produce the maximum force over the magnetic rod detached from the piston head. The control hardware was an electronic switch (based on low resistance MOSFET) designed to handle the high currents required by the experiment.

Fig. 1(c) shows the expansion/compression chamber, given by a Pyrex glass tube of 2.5 mm wall thickness, 2.6 cm inner diameter and 10.5 cm long. The entire cylindrical cavity was sealed using four O-rings located in pairs on each piston. The pressure variations inside the cylinder were recorded by a PZT hydrophone (Hyd) mounted on the lower piston. The vertical displacement of the upper piston was determined using an infrared photosensor whose analog (continuous) signal was partially interrupted by the flap mounted on the steel the magnetic rod (see Fig. 1(c)). This tracking method had a spatial resolution of ~ 2 μm and a temporal resolution of 10 μs.

In this experimental device, the bubble collapse is forced with high pressure pulses generated by the impact of a bar (from now on the "impact bar") propelled through the steel tube described in Fig. 2. This bar was made of nylon polyamide 6 (density $\rho_b = 1.14$ g/cm^3) with a mass of 23.5 g (Fig. 1(d)). The bar had a pattern of grooves employed to monitor the temporal evolution of its displacement, velocity (v_b) and acceleration (a_b) using a series of photosensors distributed along the tube (Fig. 2). The impact bar was propelled employing the compressed air injection system shown in Fig. 2(a). The gas flow and the air line pressure (P_{line}) was controlled using an electronic valve and a regulator. In this mechanism, the bar was released with a second electromagnet synchronously with the opening of the gas valve. The bar impact speed could be changed by modifying P_{line}, or by delaying the moment when the gas is released (relative to the time of flight of the bar). Both the control and synchronization systems, as well as the data acquisition from the sensors, were implemented in an Arduino UNO board with a temporal accuracy of ~ 1 μs. Tracking the position of the impact bar allowed the magnetic actuator to be deactivated just before the collision with the piston and optimize the momentum transfer from the bar to the piston.

The bubbles were generated by focusing a high power laser pulse (Nd-YAG Quantel YG980, 9 ns pulse width, $\lambda = 532$ nm) to the center of the compression chamber. The radius R_0 (defined relative to atmospheric pressure) could be set by seeding the bubbles at different instants of the traction/compression cycle or by changing the energy in the laser pulse [8,28,29]. The initial pressure p_0^{min} could be controlled by modifying the force exerted on the piston according to the polarity and intensity of the magnetic pulse in the linear actuator. The latter is the (positive) vacuum absolute pressure which determines R_{max}. Thus, bubbles could be generated by applying vacuum pressure on the system to have low values of R_0 and achieve large expansion rates ($R_{max}(p_0^{min})/R_0$).

The cavitation bubbles were characterized using two methods, one based on video recordings and the other on light scattering. In the laser induced bubble trials, images were captured with a Hitachi KP-F120 video camera, applying a stroboscopic backlighting technique with a

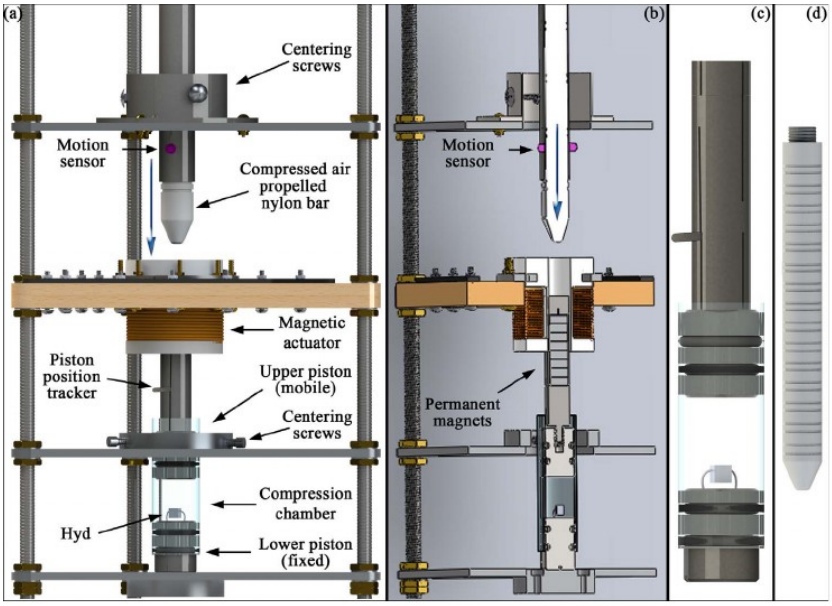

Fig. 1. Scheme of the principal components of the SFBC device. (a) Metallic structure on which the magnetic actuator and the compression chamber are mounted. (b) Cross-sectional view of the device. (c) Expansion/compression chamber together with the lower fixed piston, and the mobile upper magnetic piston. (d) Ribbed impact nylon bar with a metallic upper end (to magnetically hold it in its initial position).

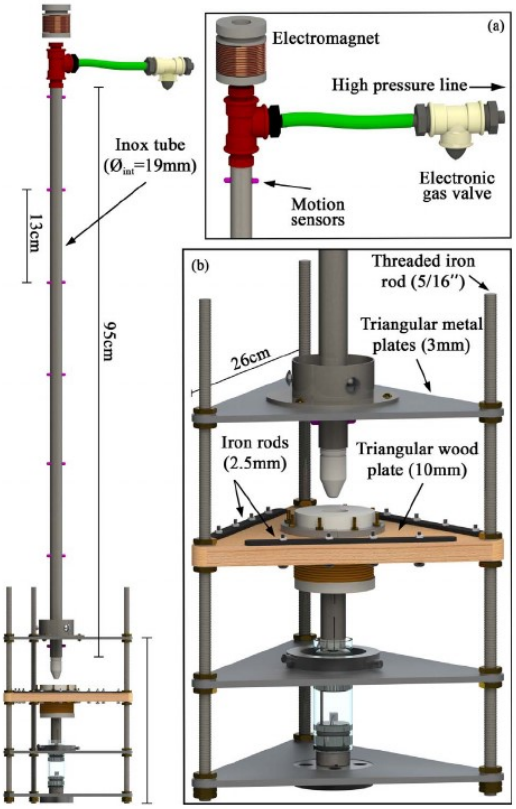

Fig. 2. Experimental device designed to produce forced collapses of laser induced cavitation bubbles. (a) Release and acceleration system. The projectile (bar) is initially held by a electromagnet and then propelled through a 19 mm tube by compressed air. (b) Detail of the structure where the different components of the system are mounted.

frequency of 206 Hz (~ 4.9 ms between flashes) [17]. These kind of measurements were useful to evaluate R_{max},R_0 and the shape stability of the LIB bubbles. In the SFBC experiments, the equilibrium radius R_0 was computed from the observed terminal velocity of ascension V_{term} of the bubbles, the liquid kinematic viscosity ν_l, and the gravity acceleration g, using the Stokes law [18]

$$R_0 = \sqrt{\frac{9\,V_{term}\,\nu_l}{2g}}. \tag{1}$$

In addition, the $R(t)$ was measured using the standard Mie scattering technique [30–32] by means of a He-Ne Melles-Griot laser (30 mW, $\lambda = 632.8$ nm). In this method the oscillating bubble was illuminated with the laser beam, and the scattered light was measured with a phototube (Oriel 77340) located near the Brewster's angle. For this particular scattering angle (85° from the forward direction) the collected light intensity is proportional to $R^2(t)$. In the experiments presented in this manuscript the scaling of the measured Mie data was performed through a numerical fit of the bubble $R(t)$, as detailed in the following section.

2.2. Bubble dynamics modelling

The radial bubble dynamics were modeled by a numerical solution of the Rayleigh-Plesset-Keller equation (RPK) [1,33] shown in Eq. (2), assuming a van der Waals gas (Eq. (3)):

$$\left(1-\frac{\dot{R}(t)}{c_{s,l}}\right)\rho_l R(t)\ddot{R}(t) + \frac{3}{2}\rho_l \dot{R}^2(t)\left(1-\frac{\dot{R}(t)}{3c_{s,l}}\right) = \left(1+\frac{\dot{R}(t)}{c_{s,l}}\right)\left[p_g(t)-p_0-p_{ext}(t)-\frac{4\mu_l \dot{R}(t)}{R(t)}-\frac{2\sigma_l}{R(t)}\right] + \frac{R(t)}{c_{s,l}}\frac{dp_g(t)}{dt}, \tag{2}$$

where p_{ext} represents an arbitrary variation in the liquid pressure, p_0 is the ambient pressure, $c_{s,l}$ is the sound speed in the liquid and ρ_l,μ_l and σ_l are the liquid density, viscosity and surface tension, respectively. This model accounts to first order for liquid compressibility, sound radiation from the oscillating bubble, the effect of the viscosity and surface tension. The pressure of the gas trapped inside the bubble p_g is related with

its volume by the expression in Eq. (3), which considers the van der Waals excluded volume [1,34]:

$$p_g(t) = \left(p_0 - p_v + \frac{2\sigma_l}{R_0}\right)\frac{(R_0^3 - h_{hc}^3)^\gamma}{[R(t)^3 - h_{hc}^3]^\gamma}, \quad (3)$$

where h_{hc} is the van der Waals hard core radius ($h_{hc} = R_0/8.86$ for argon), γ is the polytropic index and p_v is the vapor pressure (taken as a constant). In this model both the pressure and the density of the gas are assumed to be uniform in the bubble interior.

Mass transfer through the bubble wall is mainly produced by two mechanisms, evaporation and condensation. During the expansion phase, the liquid vapor and gas is diffused towards the bubble interior, and when the collapse occurs the bulk of these particles are condensed due to the high pressures and leave the bubble. The amount of vapor/gas effectively transferred across the gas/liquid interface in one cycle of expansion and collapse is rather limited, as discussed in both theoretical [35,9,36,37] and experimental investigations [38,39]. The time period needed to produce appreciable changes on the bubble size are much longer that the time scale of the driving cycle, even when liquids with a relatively high vapor pressure (like water) are used. Therefore, using low vapor pressure liquids, such as phosphoric acid, and low concentrations of a noble gas, diffusion processes and potential chemical reactions were found to be negligible, and then not included in the analysis. Results from Refs. [2,25] were reproduced in order to check the code and consistency between models.

In this work, the experiments were made with an aqueous solution of glycerol at 90% *w/w* (GL90) or phosphoric acid at 100% *w/w* (PA100) with 10–100 mbar of argon dissolved on it (van der Waals constants a = 1.355 L^2 bar/mol^2 and b = 0.03219 L/mol). The physical properties of both working fluids are detailed in Table 1. The ambient pressure in the fluid was 925 mbar (atmospheric pressure in Bariloche, Argentina). Both liquids were chosen because of their high viscosity, which prevent the effects of the RTI.

2.3. Characterization of the system main components

The magnetic actuator design was assessed taking into account electromagnetic, thermal and mechanical aspects. The dimensions and geometry of the coil were optimized using a numerical code developed by Robertson et al. [43], under the premise of maximizing the force exerted by minimizing the power required. The force developed by the magnetic actuator $|\overrightarrow{F_C}|$ was characterized using a load cell *BSL MTS-1* by varying the magnetic rod position relative to the center of the coil (z_r) and also changing the current amplitude in the winding (I_C). These studies were used as guidelines to determine the value of z_r which produced the greatest Force/Current ratio ($|\overrightarrow{F_C}|/I_C$). The maximum value of force per unit of current measured was $|\overrightarrow{f_C}^{max}| = 0.234$ N/A. The thermal behaviour of the coils was also monitored, finding that for a rectangular pulse with a 125 ms width and an amplitude of 360 A, its temperature increased by ~ 1.3 °C in each execution. The coil thermal decay time was about 3 min.

Due to the high degree of synchronization required, the system response times and the temporal evolution of the bar position ($x_b(t)$) as a function of P_{line} were studied. The projectile reached a limiting speed in a time inversely proportional to the line pressure. In this device, the range of speeds that the impact bar could take ranged from 3 m/s ($P_{line} = 0.4$ bar) to 30 m/s ($P_{line} = 2.6$ bar). Then, the bar kinetic energy could vary from 0.1 J to 10.2 J as shown in Fig. 3. A consistent repeatability of these measurements was observed. The dispersion in the time of impact, or time of flight t_{imp}, decreased considerably as P_{line} was increased, with a standard deviation in t_{imp} of 40 μs for $P_{line} = 0.4$ bar and lower than 6 μs for $P_{line} > 1.8$ bar. With these observations, the entire system was synchronized to activate the magnetic actuator for the minimum time required by the bubble to reach its maximum expansion (~ 125 ms), avoiding unnecessary diffusion of water vapor into the bubble and an overheating of the actuator.

Table 1
Physical properties of concentrated phosphoric acid 100% *w/w* and a glycerin aqueous solution 90% *w/w* at 293 K [40–42].

Substance	PA100	GL90
Vapor pressure (p_v) [Pa]	3.8	733
Density (ρ_l) [kg/m^3]	1860	1235
Sound speed (c_{sl}) [m/s]	1800	1920
Dynamic viscosity (μ_l) [Pa s]	0.26	0.22
Surface tension (σ_l) [N/m]	0.08	0.064

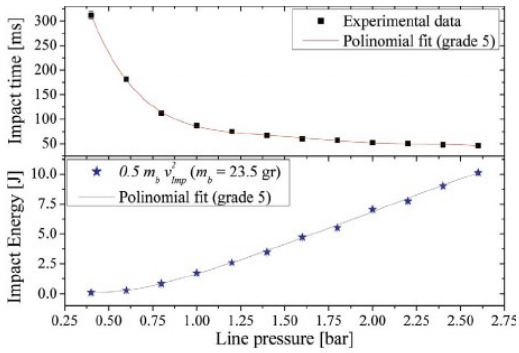

Fig. 3. Time of flight and impact energy of the propelled bar for different line pressures. The vertical statistical variation in the data is smaller than the point size, while the error in the line pressure was 0.05 bar. The impact time was fitted as a function of P_{line} using an *ad hoc* fifth degree polynomial model.

3. Results and discussion

The performance of the device was tested by a set of experiments. In detail, Section 3.1 describes how LIB bubbles at constant hydrostatic pressure were produced in order to measure the dynamics of bubbles with purely inertial collapses as a reference case. In Section 3.2, we present experimental results on SFBC in GL90 and PA100 obtained for low impact energies (i.e. low v_b). Only moderate power SFBC assays were performed in the experiments, since the glass tube forming the test section allows optical access to its interior, but was not prepared to withstand high pressures inside. Initially, we studied the device performance in the absence of bubbles and these results were used to analyze the bubble dynamics. Finally, numerical simulations of the radial dynamics of typical bubbles, performed to evaluate the system potential in situations of higher compression, are detailed in Section 3.3.

3.1. Laser cavitation at constant hydrostatic pressure

We began studying cavitation bubbles in a cuvette at fixed p_0. For this purpose, the characteristics of the inertial collapse of bubbles generated with $p_0 \simeq 10$ mbar in concentrated phosphoric acid at 100% *w/w* were observed. A typical laser induced bubble generated under the previous conditions is shown in Fig. 4(a). The picture shows four stages of the growth and collapse cycle of a LIB bubble: the generation of the bubble by a laser beam, the maximum growth of the bubble (R_{max}), one afterbounce and the bubble at its equilibrium radius (R_0). The maximum intensity of the laser beam was usually distributed over a waist of about 1 mm long [7,23], mainly due to the effect of diffraction and optical aberrations. This initial inhomogeneity induced an anisotropy in the bubble whose predominant mode matches $n = 2$ of the shape instability [44], and can produce the bubble rupture in the collapse preventing the formation of hot plasma in its interior. The low static

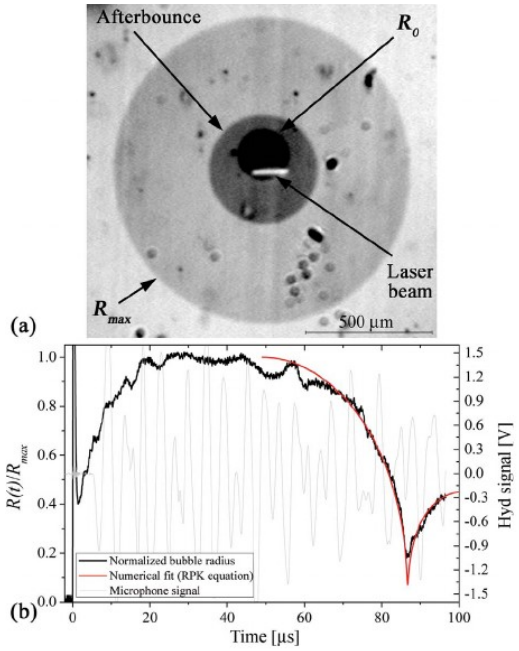

Fig. 4. Bubble radius temporal evolution of laser induced bubbles (LIB). (a) The photograph (taken using stroboscopic backlighting) shows four stages of the growth and collapse of a LIB bubble (indicated by arrows) in PA100 at a pressure of ~ 10 mbar. Those are: the laser beam generating the bubble, $R_{max} \sim 1.2$ mm, one afterbounce and R_0. (b) $R(t)$ of a LIB bubble in GL90 with a fixed $p_0 \sim 1$ bar. The experimental $R(t)$ was fitted using the RPK numerical model. The parameters obtained from the fit were $R_0 = (56 \pm 4)\,\mu$m, $R_{max} = (265 \pm 5)\,\mu$m and $\dot{R}_{max} = -80$ m/s.

pressure in the cavitation zone allowed us to create large bubbles and evaluate their degree of sphericity. The typical R_{max} of these bubbles was ~ 1.2 mm and their cavitation time was ~ 4 ms.

Subsequently, the characteristics of bubbles generated at atmospheric pressure with different laser powers were studied using GL90. Here, the threshold value in the pulse energy needed to generate a single bubble was also determined [1]. Fig. 4(b) displays a typical $R(t)$ of a LIB bubble for atmospheric pressure conditions. There, the Nd-YAG laser pulse can be distinguished as a narrow peak at $t = 0$. The explosive bubble expansion is followed by a purely inertial collapse [45], with no light emission, and a series of afterbounces of downward amplitude.

3.2. Cavitation bubbles with a single forced collapse

To evaluate the SFBC system time response and the pressure pulse shape, we ran preliminary measurements in absence of cavitation bubbles in the compression chamber. The dataset produced in this trials was crucial to further characterize the experimental setup performance and design accurate numerical simulations. As detailed in Section 2, five principal parameters were measured during the SFBC experiments: the impact velocity of the rod (v_b), the upper piston position (z_p), the hydrophone signal, proportional to the liquid pressure near the PZT, the $R(t)$ of the bubble, and its terminal ascension velocity to estimate R_0. In the measurements of Section 3.2, we used $P_{line} = 0.5$ bar, giving $v_b = 3.7$ m/s (161 mJ). The kinetic energy applied to the impact bar in these experiments is less than 1% of the total available, consequently, the collapse strength of the bubbles was not enough to produce light emission.

3.2.1. Device performance in absence of bubbles

As discussed in the following sections, the radial dynamics of the cavitation bubbles in the SFBC experiments was found to be directly linked to the pressure ramp produced by the collision of the bar. Thus, it was necessary to study the main characteristics of the liquid pressure raise in absence of cavitation bubbles.

Fig. 5 shows the evolution of $z_p(t)$ and the Hyd signal for two typical situations: the piston movement after the magnetic actuator was turned off (Fig. 5(a)) and the compression dynamics after the impact of the nylon bar (Fig. 5(b)) with the piston at its equilibrium position. The piston behaviour, once released from the magnetic pull, was studied to synchronize its descent with the bar impact. Fig. 5(a) describes the deactivation of the actuator indicated by an artifact (step-shaped at t = 0) in the Hyd signal, produced by the sudden change of the magnetic field in the coil. Once the descent of the piston begins, it reaches the extreme position after approximately 1 ms. In the same way, we characterized the response of the system to the hit of the bar for a range of velocities from 1 m/s to 4 m/s which corresponds to impact energies ranging from 12 mJ to 188 mJ. Immediately after the impact, the upper piston descends a few microns and a rebound occurs mainly due to the elasticity of the rubber O-rings. In all these cases, a consistent repeatability in $z_p(t)$ and the Hyd signal was observed.

As detailed in Fig. 5(c), during collision, the hydrophone signal (and then the liquid pressure) could be modeled as a sinusoidal ramp (red line) with a typical rise time of $\Delta t_p \sim 130\,\mu$s for the analyzed range of impact energies. The repeatability in the shape of this signal was excellent, while its amplitude grew linearly with the impact energy in the studied range. This sinusoidal model was used to perform numerical fits of the measured $R(t)$, and also complementary simulations of the bubble dynamics for a range of parameters beyond the experimentally studied at the present work.

To maximize the transfer of momentum from the projectile to the piston, the impact time of the bar (t_{imp}) was synchronized with the instant of deactivation of the actuator (t_{act}). Therefore, t_{imp} was shifted in steps of 80 µs in a range of 1 ms, taking the temporal reference when the magnetic actuator was turned off. It was considered that t_{imp} has an optimum value when a maximum amplitude in the hydrophone signal was reached (i.e. a maximum in the fluid pressure). Representative examples of these measurements are shown in Fig. 6. Fig. 6(a) shows the behaviour of the system in a complete operating cycle for a typical case. When the impact occurs, the downward movement of the upper piston is clearly boosted, this being evidenced by a change in the slope of the displacement curve, before $t = 500\,\mu$s, and an abrupt increase in the liquid pressure registered by the hydrophone. After maximum compression is reached, the piston oscillates in a decreasing amplitude regime. In panels b, c and d of Fig. 6, the response of the system is shown for different impact phases. In detail Fig. 6(b) describes how the bar strikes when the actuator is still energized, where a significant part of the impact energy is lost due to the resistance caused by the magnetic force. In Fig. 6(d), the bar strikes near the lower part of the piston excursion, thus the impact occurs when an eventual SFBC would be partially compressed, decreasing the energy transfer. It is worth noting that in the cases described above, the amplitude reached by both the Hyd signal and the piston displacement are relatively small. Conversely, these quantities are maximized in the measurement displayed in Fig. 6(c). These measurements indicate that the momentum transfer is maximum if the bar impact occurs when the upper piston is displaced approximately 10% of its total trajectory ($\Delta z_p = z_{p,max} - z_{p,min}$).

3.2.2. SFBC in a glycerin aqueous solution 90% w/w

Once the device was set up, its performance was evaluated through SFBC experiments. As previously described, the bubble collapse was not purely inertial in the forced case, but it was affected by the pressure ramp (Fig. 5(c)).

Typically, the time required for the system (piston and bubble) to reach the equilibrium position in the expansion phase is approximately

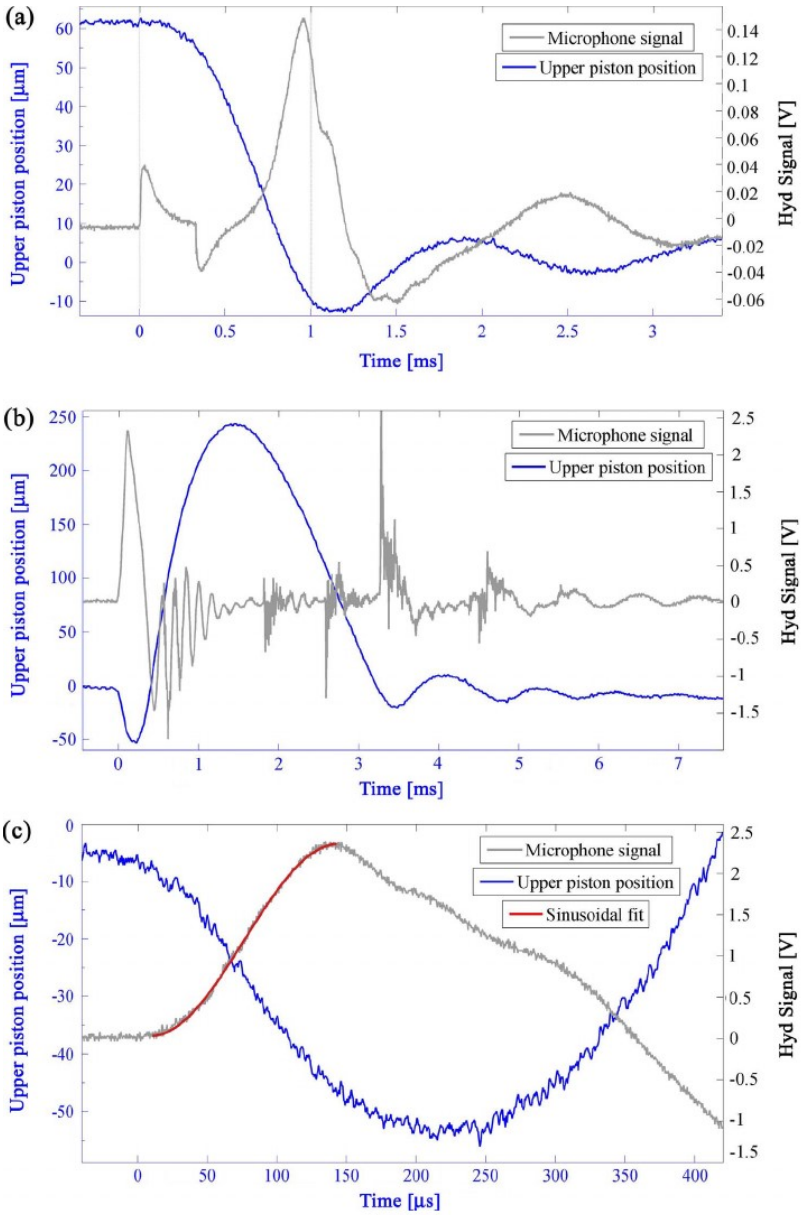

Fig. 5. Displacement of the upper piston and hydrophone signal for different types of excitation in GL90. (a) Relaxation dynamics of the piston after the magnetic actuator is deactivated. (b) Compression dynamics of the upper piston (initially in equilibrium) after receiving the impact of the bar. Here the projectile strikes the piston with a velocity of ~ 3.7 m/s (161 mJ). (c) Detail of the time interval immediately after impact shown in (b). The sinusoidal fit of the Hyd signal was used to estimate the temporal evolution of the pressure ramp within the tube.

125 ms (much longer than the magnetic actuator response time). This time value is the minimum required that the magnetic actuator must be active for the bubble to achieve its maximum expansion. The equilibrium radius and the expanded state of a typical bubble in a glycerin aqueous solution 90% w/w are shown in the photographs of Fig. 7(a). Here, R_0 was (440 ± 20) µm and the expansion ratio was close to 3. The compressive dynamics of the bubble was also characterized by measuring the $R(t)$ as shown in Fig. 7. Fig. 7(b) shows a change in the slope of z_p at the instant of impact of the bar (set as $t = 0$). In Fig. 7(c), the radius variation was relatively low for negative times even though, the actuator was turned off and the upper piston descending, while the collapse occurred in only tens of microseconds for positive times. After the main collapse, there were several afterbounces of decreasing amplitude. As long as the piston is compressing the liquid, the bubble maintains a radius close to R_{min}, but it undergoes an abrupt expansion if the piston begins to ascend. In addition, the maximum radius reached by the bubble in this second expansion could be even higher than that reached under the magnetic actuator pull, but the second collapse speed was found to be significantly lower than that in the forced case due to the low pressure caused by the piston recoil.

The effect of a bubble collapse on the hydrophone signal is given by the high frequency waves shown in Fig. 7(d). The onset of this signal occurs about 10 µs after the main bubble collapse. This delay is compatible with the time required for a signal produced by the shock wave

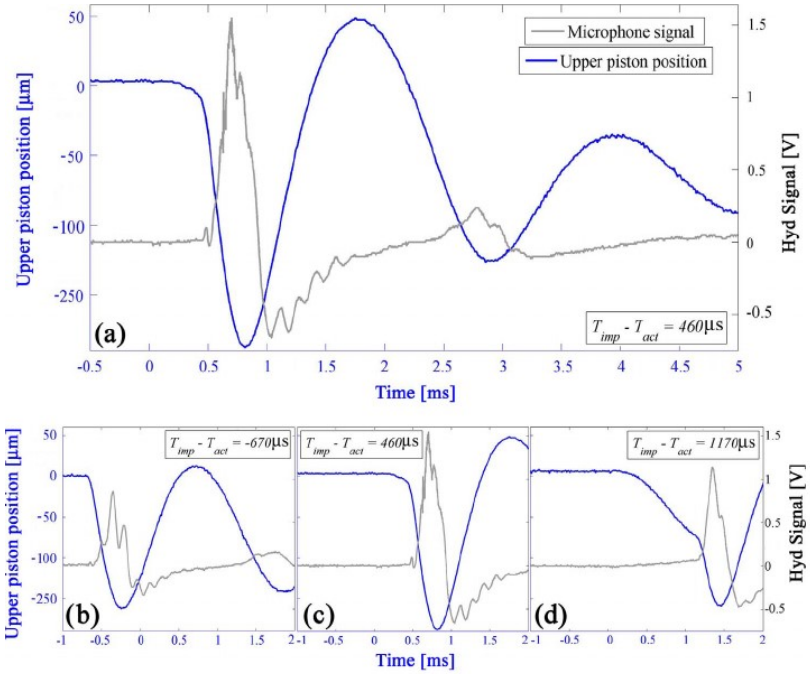

Fig. 6. Synchronization of the bar impact with the deactivation of the magnetic actuator. The hydrophone signal has a maximum when the bar hit the upper piston at the instant it had descended ~ 10% of its total path as in (c). Here v_{ib} was 3.7 m/s.

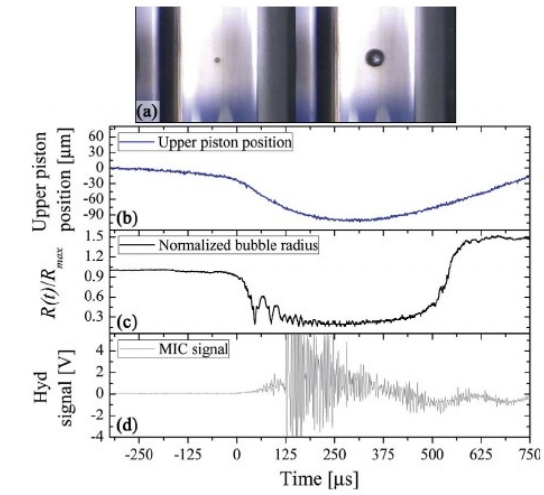

Fig. 7. Bubble dynamics of an argon bubble in the SFBC experiment using GL90. (a) Photographs of a bubble at $R_0 = (440 \pm 20)\,\mu m$ (left) and later at $R_{max} = (1.26 \pm 0.02)$ mm. (b) Temporal evolution of the piston position ($v_b = 3.7$ m/s). The zero of z_p was taken at the piston initial position. (c) Normalized $R(t)$. The temporal reference ($t = 0$) was set at the instant of impact of the bar. The bubble analyzed in this case had $R_0 = (421 \pm 20)\,\mu m$. (d) Hydrophone signal.

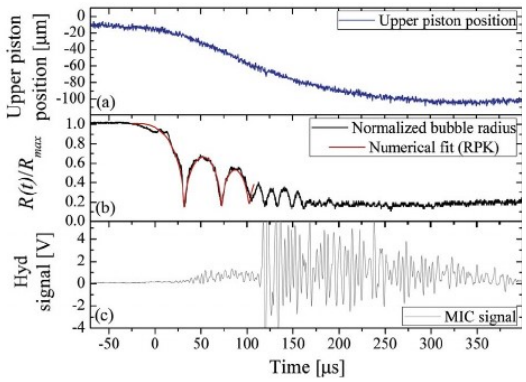

Fig. 8. Detail of a bubble collapse induced by a pressure pulse generated with $v_b = 3.7$ m/s in GL90. The temporal and spatial references are the same as those used in Fig. 7. From the numerical fit of the $R(t)$: $R_0 = (427 \pm 10)\,\mu m$, $R_{max} = (890 \pm 30)$, $\dot{R}_{max} = -126$ m/s, $\Delta t_P = (140 \pm 10)\,\mu s$ and $P_{max} = (18.5 \pm 0.5)$ bar.

emitted by the bubble to travel trough the liquid column until reaching the hydrophone. A second signal, with an amplitude 5 times greater than the first one, is originated by the collapse of a larger bubble formed by the gas remaining from previous shots of the device. This type of wave pattern is typically observed in the collapse of sonoluminescent bubbles in acoustic resonators [46]. The main collapse of the bubble and subsequent afterbounces are shown with higher detail in Fig. 8 including a numerical fit of the $R(t)$.

As a way to compare the violence of the inertial collapses (laser cavitation) with the ones produced by forced cavitation, we weighed out the time it takes for the radius of the bubble to be compressed 20% in the last section of the collapse. This criterion was set *ad hoc* considering that in non linear bubble dynamics, the raise in the gas temperature occurs in the final part of the collapse, where the thermal processes are nearly adiabatic. This analysis was carried out for multiple measurements made using $v_b \sim 3.7$ m/s, finding that the average collapse speed (near R_{min}) was 55% greater in the forced case. Simulations showing that this difference is considerably greater for larger bar impact energies are presented in Section 3.3.

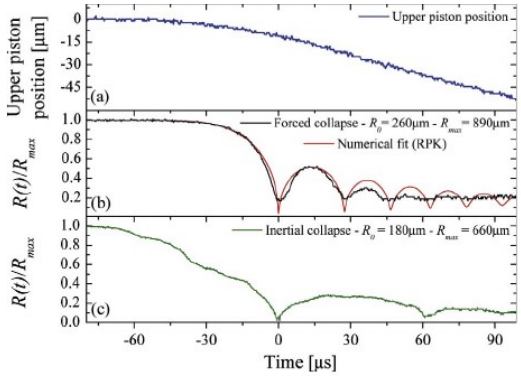

Fig. 9. Temporal evolution of SFBC ((a) and (b)) and LIB bubbles ((c)) in PA100. In the graphs (a) and (b) the bar hits the piston with $v_b \sim 3.7$ m/s. From the numerical fit: $R_0 = (260 \pm 10)\,\mu$m, $R_{max} = (890 \pm 30)\mu$m, $\dot{R}_{max} = -390$ m/s, $\Delta t_P = 110\,\mu$s and $P_{max} = 25$ bar. The laser cavitation bubble presented in (c) has $R_0 = (180 \pm 20)\,\mu$m and $R_{max} = 660\,\mu$m at a fixed $p_0 \sim 1$ bar.

3.2.3. SFBC in concentrated phosphoric acid

The experimental device for SFBC was also used to study argon bubbles in concentrated phosphoric acid (100% w/w). In Fig. 9 two measurements of the $R(t)$ of bubbles in PA100 are compared. One of them describes a forced case (Fig. 9(a) and (b)) while the other shows a purely inertial collapse (Fig. 9(c)). The SFBC bubble temporal evolution was fitted with the RPK numerical model to estimate the bubble dynamical parameters. The fitting parameters were initialized using the information obtained from video recordings. The initial pressure of the liquid surrounding the bubble (P_0^{min}), was computed with the expansion ratio (R_{max}/R_0; usually, $R_{max}/R_0 \simeq 3$) while R_0 was obtained by means of the Stokes law [17] and then used as a seed in the numerical fits. Both cases produced consistent values. The initial value of the duration of the pressure ramp (Δt_P) was estimated from the measurements of the hydrophone signal shown in Fig. 5 (i.e. $\Delta t_P = 110\,\mu$s).

The bubble analyzed in Fig. 9(b) has an equilibrium radius of $R_0 = (260 \pm 20)\,\mu$m, and according to the numerical fit, it reached a maximum radius of $R_{max} = 890\,\mu$m at an initial (minimum) pressure of $P_0^{min} \simeq 38$ mbar, for an impact velocity of $v_b = 3.7$ m/s ($P_{line} = 0.5$ bar). The LIB bubble in Fig. 9(c) had a $R_0 = (180 \pm 20)\,\mu$m and $R_{max} \simeq 660\,\mu$m computed through the Rayleigh equation for an empty cavity t_c [45]. The results described in Fig. 9 show a remarkable difference in the time of collapse between the experimental data obtained using both methods (SFBC and LIB), showing that the collapse speed was significantly larger in the forced case, taking into account the smaller size of the LIB bubble and the similarity in R_{max}/R_0.

3.3. Numerical simulations

To extend the experimental results, a series of numerical simulations were made. The main interest was to determine how the collapse violence of the bubbles depends on parameters like $\dot{R}_{max}$ and the compression ratio (R_{max}/R_{min}), when the pressure amplitude of the ramps is varied. In most of the simulations, we used parameter values similar to those obtained from the numerical fit of the experimental data shown in Fig. 9 ($R_0 = 300\,\mu$m, $R_{max} = 900\,\mu$m, $P_0^{min} = 38$ mbar and $\Delta t_P = 110\,\mu$s). The simulated $R(t)$ for different pressure amplitudes are shown in Fig. 10. The time reference (t = 0) in the simulated $R(t)$ curves was set to the instant of collapse. As expected, the results exhibited a notorious increase in the slope of the curves before the collapse ($\dot{R}_{max}$) and a decrease in the minimum radius reached by the bubbles, as the amplitude of the pressure pulse (P_{max}) is increased maintaining Δt_P fixed. The afterbounces amplitude diminishes as P_{max} is raised (i.e., greater v_b) mainly because t_c is shorter than Δt_P and the high pressure is still

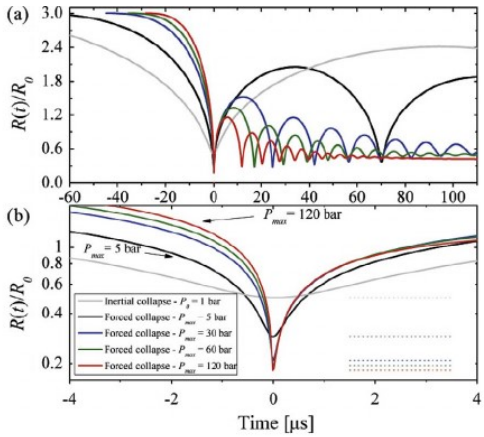

Fig. 10. Simulation of the radial dynamics of forced cavitation bubbles with different amplitudes of the pressure pulse in PA100. The simulations parameters were taken from the experimental data in Fig. 9 (i.e. $R_0 = 300\,\mu$m, $R_{max} = 900\,\mu$m, $P_0^{min} = 38$ mbar and $\Delta t_P = 110\,\mu$s). (a) This graph shows how t_c is reduced as P_{max} is increased (b) Detail of the bubble dynamics near R_{min} (indicated by the dotted lines in each case). As P_{max} is increased, the collapse velocity grows and the bubble reaches smaller R_{min}.

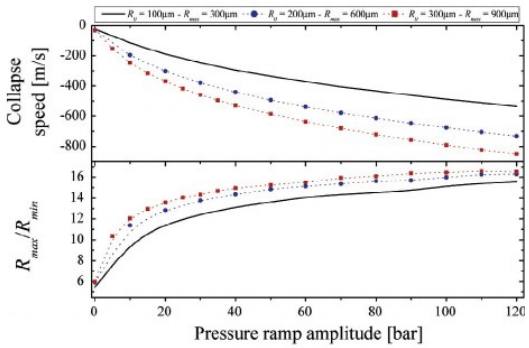

Fig. 11. Collapse speed and compression ratio of forced cavitation bubbles for different pressure pulse amplitudes. In all cases $R_{max}/R_0 = 3$, $P_0^{min} = 38$ mbar and $\Delta t_P = 110\,\mu$s.

applied during the afterbounces. The previous analysis was extended to cases with different equilibrium radius and several values of P_{max}, setting the expansion rate parameter $R_{max}/R_0 = 3$ (as observed in the experiments). The results are presented in Fig. 11. This parametric analysis indicated that for greater initial radius of the bubble (in this case R_{max}) and higher pressure, applied power in bar strike, higher values of $\dot{R}_{max}$ are obtained. Besides, the ratio R_{max}/R_{min} reaches a *plateau* at high pressures. This phenomena could be due to the fact that the minimum radius attained by the bubble cannot be smaller than the radius of van der Waals [47].

The magnitude of $\dot{R}_{max}$ usually observed in sonoluminescence using SA85 at atmospheric pressure is approximately −600 m/s [4]. In those cases R_{max}/R_{min} varies typically between 15 and 35. The results shown in Fig. 11 indicate that conditions encountered in SBSL could be replicated, and improved, using compressive pulses of an amplitude greater than 50 bar in the SFBC experiment. In the same way, the role of R_0, i.e., the amount of gas contained in the bubble, and the expansion ratio R_{max}/R_0 on the collapse strength was evaluated through simulations carried out maintaining the amplitude of the compression ramp in $P_{max} = 25$ bar and its duration of 110 μs, in agreement with the observed in Section 3.2.1. In the first case, presented in Fig. 12(a), we established a fixed ratio $R_{max}/R_0 = 3$ while R_0 was varied between 10 μm and

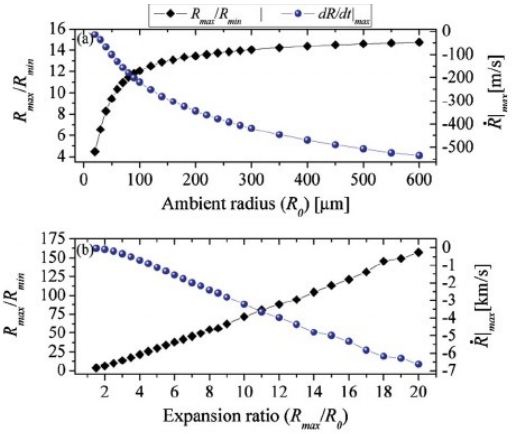

Fig. 12. Numerical simulations of the collapse speed and the compression ratio of SFBC bubbles with P_{max} = 25 bar, P_0^{min} = 38 mbar and Δt_P = 110 μs. (a) Effect of varying R_0 maintaining R_{max}/R_0 = 3 fixed. (b) Effect of the expansion ratio for a case with R_0 = 200 μm.

500 μm. The results suggest that seeding bubbles much larger than ~ 250 μm does not lead to a considerable improvement (in this particular case), since both indices (R_{max}/R_{min} and $\dot{R}_{max}$) do not change considerably for higher R_0. In the second case, R_{max}/R_0 was varied by changing R_{max} to a fixed value of R_0 = 250 μm (Fig. 12(b)). In the experiment this could be done by increasing the pull force of the piston. The simulations indicate that there is a linear rise in R_{max}/R_{min} and $\dot{R}_{max}$ as R_{max}/R_0 was increased. This is particularly important, since it shows how a significant upscale in the collapse strength could be achieved by increasing the expansion ratio, without the need of applying high compressive pressures, which might be difficult to implement experimentally. It should be pointed out that these simulations provided information about the behaviour of the system, although its validity for the highest values of R_{max}/R_0 may be limited by the bubble rupture, which was not considered for these calculations.

4. Conclusions

In this work, a new method to produce controlled collapses of cavitation bubbles was presented. It is based on an electromechanical device designed to manipulate bubbles in a single forced collapse (SFBC), and brings several advantages with respect to acoustically driven systems, laser cavitation or a conventional water hammer device. The main improvement over previous cavitation systems is that it introduces the possibility to expand and stabilize the shape of the bubbles before collapse in a fully controlled way. This, in turn, increases mechanical energy concentration and reduces the development of shape related instabilities which lead to a bubble rupture. Moreover, this new methodology allows independent manipulation of relevant dynamical bubble parameters that determine the collapse violence such as R_{max},R_0,p_0^{min},p_0^{max} and t_c.

Laser cavitation (LIB) and SFBC experiments were performed on a glycerin aqueous solution (90% *w/w*), as well as concentrated phosphoric acid (100% *w/w*). A comparative analysis of the parameters related to the energy concentration, such as the collapse speed and the compression ratio, demonstrated that forced collapses are notoriously more violent than purely inertial ones (having both similar initial conditions).

In addition, numerical simulations were performed for prototypical bubbles collapsing under a pressure ramp by solving the RPK equation. This allowed us to study some limiting cases in the system performance and also explore optimal conditions for compressing the bubbles. The simulated results indicated that for a given R_{max}/R_0, a raise in R_{max} and the amplitude of the applied pressure ramp p_0^{max}, produced an upscale in the bubble collapse violence indicated by an increase in $\dot{R}_{max}$ and R_{max}/R_{min}, although that increment would reach a limiting value for pressures greater than approximately 100 bar. The role of the volume of gas trapped in the bubbles (i.e. R_0) and the expansion ratio R_{max}/R_0 on the collapse strength, was also evaluated through numerical simulations. The results suggested that maintaining R_{max}/R_0 and p_0^{max} fixed, an increase in R_0 produced a growth on $\dot{R}_{max}$ and R_{max}/R_{min} but their dependence on R_0 is relatively weak. We found that the most relevant parameter related to the collapse violence was the initial expansion ratio. For a constant value of R_0,p_0^{max} and t_c, the collapse velocity increased almost proportionally to R_{max}/R_0. Furthermore, in the proposed experimental setup, this parameter could be easily adjusted by changing the magnetic actuator configuration before the impact of the bar.

The device potential has not been fully exploited. Consequently, some modifications in the design and a larger number of experiments are required in order to explore the limits of the energy concentration achievable on a bubble collapse. In particular, it is necessary to replace the expansion/compression chamber with a more resistant vessel to hold higher pressures. A viable alternative could be a steel pressure chamber with quartz or laminated glass windows. On the other hand, the use of an ultrasound field applied to the tube could be explored to stabilize the existing bubbles and force their coalescence at a fixed location. Furthermore, this would be particularly useful when the laser shot produces multiple bubbles [22], enabling the use of the same bubble in several executions of the device.

It can be concluded that the use of this experimental method involving the previous expansion of the bubble before the impulsive compression is a promising strategy that deserves more research.

Acknowledgements

We are deeply grateful with Pablo García Martínez for his useful comments and the significant contribution that he made on the numerical model setup. We also thank Olivia Borgue for making most of the CAD drawings presented in this paper and Fernando J. Rosselló for proof reading this manuscript. J.M.R. was supported with a postdoctoral scholarship granted by CONICET.

References

[1] W. Lauterborn, T. Kurz, Physics of bubble oscillations, Rep. Prog. Phys. 73 (2010) 106501.
[2] B. Kappus, S. Khalid, S. Putterman, 100-Watt sonoluminescence generated by 2.5-atmosphere-pressure pulses, Phys. Rev. E. 83 (2011) 56304.
[3] M. Ramsey, R. Pitz, Energetic cavitation collapse generates 3.2 Mbar plasma with a 1.4 J driver, Phys. Rev. Lett. 110 (2013) 154301.
[4] J.M. Rosselló, D. Dellavale, F.J. Bonetto, Energy concentration and positional stability of sonoluminescent bubbles in sulfuric acid for different static pressures, Phys. Rev. E 88 (2013) 033026.
[5] C.-D. Ohl, O. Lindau, W. Lauterborn, Luminescence from spherically and aspherically collapsing laser-induced bubbles, J. Acoust. Soc. Am. 103 (1998) 3077.
[6] O. Baghdassarian, B. Tabbert, G. Williams, Luminescence characteristics of laser-induced bubbles in water, Phys. Rev. Lett. 83 (1999) 2437–2440.
[7] O. Lindau, W. Lauterborn, Laser-produced cavitation studied with 100 million frames per second, in: AIP Conf. Proc., AIP, 2000, pp. 385–388.
[8] B. Wolfrum, T. Kurz, O. Lindau, W. Lauterborn, Luminescence of transient bubbles at elevated ambient pressures, Phys. Rev. E. 64 (2001) 46306.
[9] I. Akhatov, O. Lindau, A. Topolnikov, R. Mettin, N. Vakhitova, W. Lauterborn, Collapse and rebound of a laser-induced cavitation bubble, Phys. Fluids 13 (2001) 2805.
[10] I. Akhatov, N. Vakhitova, A. Topolnikov, K. Zakirov, B. Wolfrum, T. Kurz, O. Lindau, R. Mettin, W. Lauterborn, Dynamics of laser-induced cavitation bubbles, Exp. Therm. Fluid Sci. 26 (2002) 731–737.
[11] O. Lindau, W. Lauterborn, Cinematographic observation of the collapse and rebound of a laser-produced cavitation bubble near a wall, J. Fluid Mech. 479 (2003) 327–348.
[12] E. Brujan, D. Hecht, F. Lee, G. Williams, Properties of luminescence from laser-created bubbles in pressurized water, Phys. Rev. E 72 (2005) 66310.
[13] O. Baghdassarian, B. Tabbert, G. Williams, Luminescence from laser-created bubbles in cryogenic liquids, Phys. Rev. E 75 (2007) 66305.
[14] E.M. Englert, A. McCarn, G.a. Williams, Luminescence from laser-induced bubbles

in water-glycerol mixtures: effect of viscosity, Phys. Rev. E 83 (2011) 46306.
[15] B. Li, H. Zhang, J. Lu, X. Ni, Experimental investigation of the effect of ambient pressure on laser-induced bubble dynamics, Opt. Laser Technol. 43 (2011) 1499–1503.
[16] R. Sadighi-Bonabi, F. Razeghi, H. Ebrahimi, S. Fallahi, E. Lotfi, Quasiadiabatic approach for laser-induced single-bubble sonoluminescence, Phys. Rev. E 85 (2012) 16302.
[17] L. Rechiman, F.J. Bonetto, J. Rossell, Effect of the Rayleigh-Taylor instability on maximum reachable temperatures in laser-induced bubbles, Phys. Rev. E 86 (2012).
[18] G. Batchelor, An Introduction to Fluid Dynamics, Cambridge University Press, Cambridge, UK, 1967.
[19] C. Ohl, Luminescence from acoustic-driven laser-induced cavitation bubbles, Phys. Rev. E. Stat. Phys. Plasmas Fluids. Relat. Interdiscip. Top. 61 (2000) 1497–1500.
[20] T. Kurz, T. Wilken, D. Kroninger, L. Wimann, W. Lauterborn, B. Enflo, C.M. Hedberg, L. Kari, Transient dynamics of laser-induced bubbles in an ultrasonic field, AIP Conf. Proc. 1022 (2008) 221–224.
[21] J.R. Sukovich, A. Sampathkumar, P.a. Anderson, R.G. Holt, Y.a. Pishchalnikov, D.F. Gaitan, Temporally and spatially resolved imaging of laser-nucleated bubble cloud sonoluminescence, Phys. Rev. E 85 (2012) 56605.
[22] J.M. Rosselló, Ph.D. Thesis, Frontera de estabilidad en sonoluminiscencia y concentración de energía en cavitación transitoria forzada, Instituto Balseiro, 2015.
[23] A. Vogel, S. Busch, U. Parlitz, Shock wave emission and cavitation bubble generation by picosecond and nanosecond optical breakdown in water, J. Acoust. Soc. Am. 100 (1996) 148–165.
[24] A. Chakravarty, T. Georghiou, T. Phillipson, A. Walton, Stable sonoluminescence within a water hammer tube, Phys. Rev. E 69 (2004) 66317.
[25] R. Urteaga, P. Garca-Martnez, F. Bonetto, Dynamics of sonoluminescing bubbles within a liquid hammer device, Phys. Rev. E 79 (2009) 16306.
[26] R. Urteaga, Ph.D. Thesis, Concentración de energía en sonoluminiscencia, Instituto Balseiro, 2008.
[27] S. Khalid, B. Kappus, K. Weninger, S. Putterman, Opacity and transport measurements reveal that dilute plasma models of sonoluminescence are not valid, Phys. Rev. Lett. 108 (2012) 104302.
[28] R. Zhao, R.Q. Xu, Z.H. Shen, J. Lu, X.W. Ni, Experimental investigation of the collapse of laser-generated cavitation bubbles near a solid boundary, Opt. Laser Technol. 39 (2007) 968–972.
[29] Y.-H. Chen, I. Lin, Dynamics of impacting a bubble by another pulsed-laser-induced bubble: Jetting, fragmentation, and entanglement, Phys. Rev. E 77 (2008) 26304.
[30] B. Barber, S. Putterman, Light scattering measurements of the repetitive supersonic implosion of a sonoluminescing bubble, Phys. Rev. Lett. 69 (1992) 3839–3842.
[31] T.J. Matula, Inertial cavitation and single-bubble sonoluminescence, Philos. Trans. Roy. Soc. A Math. Phys. Eng. Sci. 357 (1999) 225–249.
[32] B. Gompf, R. Pecha, Mie scattering from a sonoluminescing bubble with high spatial and temporal resolution, Phys. Rev. E 61 (2000) 5253–5256.
[33] J.B. Keller, M. Miksis, Bubble oscillations of large amplitude, J. Acoust. Soc. Am. 68 (1980) 628.
[34] J. Holzfuss, M.T. Levinsen, Stability of a sonoluminescing nitrogen bubble in chilled water, Phys. Rev. E 77 (2008) 46304.
[35] R. Löfstedt, K. Weninger, S. Putterman, B. Barber, Sonoluminescing bubbles and mass diffusion, Phys. Rev. E 51 (1995) 4400–4410.
[36] G.F. Puente, R. Urteaga, F.J. Bonetto, Numerical and experimental study of dissociation in an air-water single-bubble sonoluminescence system, Phys. Rev. E 72 (2005) 46305.
[37] Y. Zhang, S. Li, Mass transfer during radial oscillations of gas bubbles in viscoelastic mediums under acoustic excitation, Int. J. Heat Mass Transf. 69 (2014) 106–116.
[38] J. Lee, S. Kentish, M. Ashokkumar, Effect of surfactants on the rate of growth of an air bubble by rectified diffusion, J. Phys. Chem. B 109 (2005) 14595–14598.
[39] T. Leong, S. Wu, S. Kentish, M. Ashokkumar, Growth of bubbles by rectified diffusion in aqueous surfactant solutions, J. Phys. Chem. C 114 (2010) 20141–20145.
[40] B. Winn, Puried Phosphoric Acid Manual, first ed., PCS Sales, Northbrook, US, 2005.
[41] A. Moshaii, M. Faraji, S. Tajik-Nezhad, Study of single bubble sonoluminescence in phosphoric acid, Ultrason. Sonochem. 18 (2011) 1148–1152.
[42] D.W. Green, Perrys Chemical Engineers Handbook, eighth ed., McGraw-Hill, New York, NY, 2008.
[43] W. Robertson, B. Cazzolato, A. Zander, Axial force between a thick coil and a cylindrical permanent magnet: optimizing the geometry of an electromagnetic actuator, IEEE Trans. Magn. 48 (2012) 2479–2487.
[44] Y. Hao, a. Prosperetti, I. Introduction, The effect of viscosity on the spherical stability of oscillating gas bubbles, Phys. Fluids 11 (1999) 1309.
[45] T.G. Leighton, The Acoustic Bubble, first ed., Academic Press, 1994.
[46] J. Holzfuss, M. Rggeberg, A. Billo, Shock wave emissions of a sonoluminescing bubble, Phys. Rev. Lett. 81 (1998) 5434–5437.
[47] M.S. Plesset, A. Prosperetti, Bubble dynamics and cavitation, Annu. Rev. Fluid Mech. 9 (1977) 145–185.